THE ASTROPHYSICAL JOURNAL, 477:969–981, 1997 March 10

THE STRUCTURE AND PROPERTIES OF SOLAR ACTIVE REGIONS AND QUIET-SUN AREAS OBSERVED IN SOFT X-RAYS WITH *YOHKOH*/SXT AND IN THE EXTREME-ULTRAVIOLET WITH SERTS

JEFFREY W. BROSIUS,[1] JOSEPH M. DAVILA, ROGER J. THOMAS, AND JULIA L. R. SABA[2]
Laboratory for Astronomy and Solar Physics, Code 682, NASA/Goddard Space Flight Center, Greenbelt, MD 20771

HIROHISA HARA
National Astronomical Observatory, Mitaka, Tokyo 181, Japan

AND

BRUNELLA C. MONSIGNORI-FOSSI[3]
Arcetri Astrophysical Observatory, Largo Enrico Fermi 5, 50125 Firenze, Italy
Received 1996 May 10; accepted 1996 September 17

ABSTRACT

We observed two solar active regions (NOAA regions 7563 and 7565), quiet-Sun areas, and a coronal hole region simultaneously with Goddard Space Flight Center's Solar EUV Rocket Telescope and Spectrograph (SERTS) and with the *Yohkoh* Soft X-ray Telescope (SXT) on 1993 August 17. SERTS provided spatially resolved active region and quiet-Sun slit spectra in the 280 to 420 Å wavelength range, and images in the lines of He II λ303.8, Mg IX λ368.1, Fe XV λ284.1, and Fe XVI λλ335.4 and 360.8 SXT provided images through multiple broadband filters in both the full-frame imaging mode and the partial-frame imaging mode.

The SERTS images in Fe XV (log $T_{max} = 6.33$, where T_{max} is the temperature which maximizes the fractional ion abundance in the available ionization equilibrium calculations, i.e., the formation temperature) and Fe XVI (log $T_{max} = 6.43$) exhibit remarkable morphological similarity to the SXT images. Whereas the Fe XV and XVI images outline the loop structures seen with SXT, the cooler He II (log $T_{max} = 4.67$) and Mg IX (log $T_{max} = 5.98$) images outline loop footpoints. In addition, the Mg IX emission outlines other structures not necessarily associated with the hot loops; these may be cool ($T \lesssim 1 \times 10^6$ K) loops.

From the spatially resolved slit spectra, we obtained emission-line profiles for lines of He II λ303.8, Mg IX λ368.1, Fe XIII λ348.2, Si XI λ303.3, Fe XIV λ334.2, Fe XV λ284.1, and Fe XVI λ335.4 for each spatial position. Based upon the spatial variations of the line intensities, active region 7563 systematically narrows when viewed with successively hotter lines, and appears narrowest in the broadband soft X-ray emission. The active region width (full width at half-maximum intensity) diminishes linearly with log T_{max}; the linear fit yields an extrapolated effective log T_{max} of 6.51 ± 0.01 for the X-ray emission. The most intense, central core straddles the magnetic neutral line.

Active region and quiet-Sun one-dimensional temperature scans were derived from intensity ratios of spatially resolved SERTS slit spectral lines, and from coregistered SXT filter ratios. The highest plasma temperatures were measured in the most intense, central core of region 7563. The temperatures derived from Fe XVI λ335.4/Fe XV λ284.1 and Fe XVI λ335.4/Fe XIV λ334.2 vary significantly (based upon the measurement uncertainties) but not greatly (factors of less than 1.5) across the slit. The average log T values derived from the above two ratios for region 7563 are 6.39 ± 0.04 and 6.32 ± 0.02, respectively. Somewhat larger systematic variations were obtained from all available SXT filter ratios. The average active region log T values derived from the SXT AlMgMn/thin Al, thick Al/thin Al, and thick Al/AlMgMn filter ratios are 6.33 ± 0.03, 6.45 ± 0.02, and 6.49 ± 0.03, respectively.

Active region and quiet-Sun one-dimensional density scans were derived from intensity ratios of spatially resolved SERTS slit spectral lines of Fe XIII and Fe XIV. The derived densities show neither systematic nor significant variations along the slit in either the active region or the quiet-Sun, despite the fact that the intensities themselves vary substantially. This indicates that the product of the volume filling factor and the path length ($f\Delta l$) must be greater by factors of 3–5 in the active region core than in the outskirts. Furthermore, the derived active region densities are ~2 times the quiet-Sun densities. This density difference is adequate to explain the factor of ~4 intensity difference in Fe XII and Fe XIII between the active and quiet areas, but it is not adequate to explain the factor of ~8 intensity difference in Fe XIV between the active and quiet areas. We attribute the latter to a greater $f\Delta l$ in the active regions.

Statistically significant Doppler shifts are not detected in region 7563 or in the quiet-Sun with any of the EUV lines.

Subject headings: Sun: activity — Sun: corona — Sun: X-rays, gamma rays — Sun: UV radiation

[1] Also Hughes STX Corporation, 4400 Forbes Boulevard, Lanham, MD 20706.
[2] Also Lockheed Solar & Astrophysics Laboratory, 3251 Hanover Street, Palo Alto, CA 94304.
[3] Died unexpectedly on 1996 January 22. Her friends and colleagues miss her deeply.

1. INTRODUCTION

The Sun has been extensively observed in the extreme ultraviolet (EUV) and X-ray portions of the electromagnetic spectrum during the space age. These observations have provided information on hot coronal loops, cool coronal loops, collections of unresolvable "blobs" of coronal loops, loops which interconnect active regions, X-ray bright points, and coronal holes. In this paper, we use coordinated EUV and soft X-ray observations to describe the morphology and to measure plasma properties of several of the coronal structures listed above.

Sounding rocket observations with broadband X-ray filters revealed that the intensities of active regions peak above the photospheric magnetic neutral lines in the cores of the regions and suggested that these are the locations of the hottest plasma in the regions (Vaiana, Krieger, & Timothy 1973). Subsequent X-ray observations obtained with a variety of instrumentation confirmed this result and led to the well-known picture of loop arcades straddling the magnetic neutral lines between areas of opposite magnetic polarity. Extreme ultraviolet observations obtained with the NRL S-082A spectroheliograph on *Skylab* led to the same conclusion: that the most intense high-temperature plasmas originate in loops or systems of unresolved loops that extend across the neutral lines at the centers of active regions (e.g. Sheeley 1980, 1981).

Pye et al. (1978) obtained active region temperatures between 2.5 and 3.2×10^6 K from *Skylab* S-054 broadband X-ray filtergrams, and similar values from X-ray line spectra obtained simultaneously with a rocket-borne spectrometer. Despite the excellent agreement, Pye et al. (1978) recognized that this was the temperature range to which their instruments were most sensitive and pointed out the need for wider temperature coverage. Gerassimenko, Solodyna, & Nolte (1978), also using the S-054, obtained active region loop temperatures of $2.2–2.5 \times 10^6$ K. These values seem to be fairly characteristic of quiescent active region X-ray plasma temperatures, since similar values have been derived from sounding rocket broadband X-ray observations (e.g., Webb et al. 1987) as well from X-ray emission-line intensity ratios obtained with the X-ray Polychromator (XRP) aboard the *Solar Maximum Mission* (*SMM*) satellite (e.g., Saba & Strong 1991; Nitta et al. 1991; Brosius et al. 1992; Schmelz et al. 1992, 1994).

The launch of the Japanese *Yohkoh* spacecraft in 1991 signaled the start of a new and exciting era in solar X-ray observing. *Yohkoh* soft X-ray movies of the dynamic solar corona have captivated audiences in the scientific as well as in the lay communities, and *Yohkoh* flare observations have revolutionized our understanding of processes occurring during solar flares. However, of the three X-ray instruments on *Yohkoh*, only the Soft X-ray Telescope (SXT) (Tsuneta et al. 1991) is appropriate for observing the quiescent solar corona. With its high spatial resolution imaging capability ($\sim 2\farcs5$ in its "partial frame" imaging mode), its five broadband X-ray filters, and its high dynamic range, the SXT has repeatedly proved its worth. It is however, sensitive only to coronal plasma, and tends to measure the hottest plasma along any given line of sight. For example, Hara et al. (1992) obtained plasma temperatures of $5–6 \times 10^6$ K in active regions, and 2.7×10^6 K in quiet-Sun areas. Although the latter is consistent with results from Brosius et al. (1993, 1996) and Vernazza & Reeves (1978), the former is relatively high for an average active region temperature, in light of the temperature values quoted in the previous paragraph. Hara et al. (1992) point out that differences in the temperatures derived from different filter ratios may be a manifestation of multithermal plasma along the line of sight. It is, therefore, quite valuable to analyze SXT observations with coordinated observations which are sensitive to lower temperature plasmas. We do this in the present work.

Whereas X-ray observations are generally useful for observing only coronal plasmas, EUV observations are useful for observing both transition region *and* coronal plasmas. The S-082A spectroheliograph on *Skylab*, for example, obtained (overlapping) images in numerous emission lines, including Ne VII, Mg IX, Fe XV, and Fe XVI; these are formed at temperatures of 0.5, 1.0, 2.0, and 2.5×10^6 K, respectively. These observations revealed the general characteristics of solar multithermal plasma distributions (e.g., Tousey et al. 1973; Sheeley 1980, 1981; Bray et al. 1991 and references therein) and were used to derive temperatures and densities of coronal loops and their surrounding structures (Cheng 1980). The derived temperatures are $\sim 2–2.3 \times 10^6$ K. However, although the NRL slitless spectrograph on *Skylab* (Tousey et al. 1977) provided high spatial ($\sim 2''$) and spectral (~ 0.1 Å) resolution images in the 171–630 Å waveband, it was limited by the overlap of images from nearby spectral lines. The *Skylab* observations provided excellent diagnostic capabilities for small, intense sources like flares (e.g., Dere 1978; Dere et al. 1979), but they were less than ideal for quiet-Sun areas and quiescent active regions. Other previous solar EUV observations, obtained with the Harvard scanning spectrometer on *OSO 6* (Dupree et al. 1973), the EUV and X-ray spectroheliograph on *OSO 7* (Neupert, Thomas, & Chapman 1974), and the EUV spectrometer-spectroheliograph on *Skylab* (Vernazza & Reeves 1978), had such coarse spectral resolution ($\lesssim 0.8$ Å) that it precluded accurate determinations of coronal plasma properties from line ratio measurements in most cases. Behring et al. (1976) obtained spectra with 0.06 Å spectral resolution, but those spectra were acquired from full-Sun observations and so provide no information about distinct features on the Sun. Although the Behring et al. (1976) observations have proved very useful for providing line identifications at EUV wavelengths, the relative line intensities were only approximately calibrated, rendering line intensity ratio measurements inaccurate.

The Solar EUV Rocket Telescope and Spectrograph (SERTS) (Neupert et al. 1992b) was designed to improve upon earlier EUV instrumentation by (i) retaining the stigmatic imaging capability of the S-082A on *Skylab* while providing greater spatial selectivity so that image overlap in spectral regions with numerous emission lines would be reduced, and (ii) achieving high spectral resolution (instrumental FWHM $\sim$ 55 mÅ) with less spatial convolution than had been previously available. SERTS was designed and built at Goddard Space Flight Center. Its spectrograph entrance aperture enables both spectra and spectroheliograms to be obtained simultaneously. Spectra are obtained along a narrow slit which connects two rectangular lobes within which the spectroheliograms are imaged. Because of the relatively small area covered by the

rectangular lobes (5×8 arcmin^2), the amount of image overlap is greatly reduced from that of earlier EUV imagery (Neupert et al. 1992b). Maps in the emission lines of Fe XV at 284.1 Å, He II at 303.8 Å, Fe XVI at 335.4 and 360.8 Å, and Mg IX at 368.1 Å are generally relatively uncontaminated. By adjusting the pointing of the instrument during its flight, both images and spectra can be obtained for the same portion of the Sun.

SERTS was successfully flown in 1989 (Neupert et al. 1992a; Jordan et al. 1993; Thompson et al. 1993; Thomas & Neupert 1994), 1991 (Davila et al. 1993; Brosius et al. 1993, 1994, 1996; Falconer 1994), and 1993 (Brosius et al. 1996). The 1989 flight used a standard gold-coated toroidal diffraction grating, but the 1991 and 1993 flights incorporated a multilayer coated grating which enhanced the instrumental sensitivity over a portion of the EUV bandpass (Thomas et al. 1991; Keski-Kuha, Thomas, & Davila 1992). The 1993 flight was coordinated with *Yohkoh* SXT observations and with Very Large Array (VLA) microwave observations. Only the EUV and X-ray observations are analyzed in the present work.

The SERTS/SXT coordinated data set provides extensive temperature coverage of two active regions, one small sunspot, quiet-Sun areas, and a coronal hole. In § 2 we describe the observations; in § 3 we discuss the image morphology, EUV spectral scans, temperature, density, and Doppler shifts; and in § 4 we summarize our conclusions.

2. OBSERVATIONS

We obtained simultaneous *Yohkoh* SXT soft X-ray images and SERTS EUV spectroheliograms of NOAA active regions 7563 (S10 W15) and 7565 (S15 E20), quiet-Sun areas, and a coronal hole region around 1800 UT on 1993 August 17. Both active regions were relatively weak. Region 7565 had one small spot with a maximum photospheric longitudinal magnetic field of $\sim$1000 G and an areal coverage of 90 millionths of the visible hemisphere. Region 7563 had three smaller spots with a total areal coverage of 10 millionths of the visible hemisphere. The maximum longitudinal field in 7563 was $\sim$500 G. Magnetic field strengths were obtained from magnetograms acquired with the NASA/NSO spectromagnetograph at Kitt Peak (Jones et al. 1992), and spot areas were obtained from Solar Geophysical Data (1993). The spots in region 7563 were very small and did not manifest themselves in the form of intensity depressions in either the hot EUV emission or the X-ray emission (see Webb 1981). Spatially resolved EUV spectra of region 7563 and of quiet-Sun areas were also obtained.

2.1. *SERTS*

SERTS was launched on a Terrier-boosted Black Brant rocket from White Sands, NM, at 1800 UT on 1993 August 17, and data were recorded between 100 and 492 s after launch. The lobe-slit-lobe format of the SERTS data is easily visible in Figures 1 (Plates 26–27) and 2 (Plates 28–29). Flight data were recorded on EUV-sensitive photographic film. Four different exposures were obtained in each of two different pointing positions; this ensured the availability of optimally exposed spectral lines and spectroheliograms for both strong and weak spectral features. All data shown and used for analysis in this work are composites of optimally exposed spectra and images. Relative line intensities are accurate to within 20% over the 280–420 Å wavelength range. The spatial resolution is $\sim 5''$.

The absolute pointing of the SERTS spectrograph, and hence its reliable coalignment with *Yohkoh* SXT, was obtained by coaligning the SERTS He II λ304 images with He I λ10830 (absorption) images obtained from the NASA/NSO spectromagnetograph at Kitt Peak. This method works very well since the correlation between features seen in the two wavelengths is generally quite good (Harvey & Sheeley 1977; Thompson et al. 1993; Brosius et al. 1993). The 10830 images were rotated forward or backward in time as needed to compensate for solar rotation that is due to the time differences between the He I λ10830 and the He II λ304 observations. The formal uncertainty in the coalignment is $\sim 7''$.

Numerous emission lines are available in the SERTS slit spectra. These include lines from the eight ionization stages of iron between Fe X and Fe XVII, as well as lines from other species such as He II, Mg IX, Si XI, and Ni XVIII. These lines are formed in widely differing temperature regimes, and thus invite analyses of multithermal plasmas. Table 1 gives a list of selected ion species along with their corresponding log T_{max} values; T_{max} is here taken to be the temperature which maximizes the fractional ion abundance in the available ionization equilibrium calculations. For iron, log T_{max} is derived from quadratic fits to the ionization equilibrium calculations of Arnaud & Raymond (1992); for the other elements, it is derived from fits to similar calculations performed by Monsignori-Fossi (1992). Lists of the emission lines found in the active region and quiet-Sun spatially averaged SERTS slit spectra from the 1993 flight may be found in Brosius et al. (1996).

SERTS spectra and spectroheliograms display wavelength-dependent background levels (Thomas & Neupert 1994; Brosius et al. 1996) that are due to film fog, scattered light, and actual solar continuum. We used the spatially resolved slit spectra (from which the background is easy to remove) to derive an algorithm for removing the background from the spectroheliograms. This algorithm was applied to all of the SERTS images used in this paper. As a consistency check, the background-corrected image intensities corresponding to the location of the SERTS slit

TABLE 1

Log T_{max} VALUES FOR EUV EMISSION LINES

Ion	log T(max)
Fe X.....	5.98
Fe XI.....	6.06
Fe XII.....	6.14
Fe XIII.....	6.20
Fe XIV.....	6.27
Fe XV.....	6.33
Fe XVI.....	6.43
Fe XVII.....	6.60
He II.....	4.67
Mg IX.....	5.98
Si XI.....	6.20
Ni XVIII.....	6.52
Ca XVIII.....	6.76

were compared with the slit intensities themselves and found to be consistent within the expected uncertainties.

2.2. *Yohkoh*

Full-Sun *Yohkoh* images were obtained with the AlMgMn and thin Al broadband soft X-ray filters. Both of these images are composites of three different images taken with the same filter, each obtained with a different exposure duration in order to maximize the dynamic range. The X-ray intensity is normalized by the exposure duration, so that it is given in units of DN s^{-1}. ("DN" is the *Yohkoh* "Data Number" unit.) All *Yohkoh* images were obtained during, or within (at most 10) minutes of the SERTS flight. Dark and stray light corrections were done with the standard procedures. The *Yohkoh* images shown in Figures 1 and 2 were extracted from the composite full Sun image obtained with the AlMgMn filter. It was rescaled so that its pixel size, originally 4".91, matches that of SERTS (4".41).

Partial frame images (PFIs) of region 7563 were obtained with several different exposure times for each of the AlMgMn, thin Al, and thick Al filters. This enabled the maximization of the effective dynamic range. With their pixel sizes of 2".455 these images cover areas of 314" × 314" on the solar disk. Dark and stray light corrections were again done with the usual procedures. The partial frame images were used for all of the soft X-ray temperature analyses of AR 7563 below.

3. RESULTS

Figures 1 and 2 show *Yohkoh* SXT images which correspond, respectively, to the two SERTS pointing positions. The four frames in each figure show the same *Yohkoh* SXT image; intensity contours of SERTS images in the emission lines of Fe XVI λ335.4, Fe XV λ284.1, Mg IX λ368.1, and He II λ303.8 are superposed. The primary target active region (NOAA region 7563) is in the center of each frame in Figure 1; coronal hole areas are to the west (*right*) and quiet-Sun areas and the secondary target region (7565) are to the east (*left*). Region 7565 is the brightest area toward the left of the figure. In the first pointing position, the SERTS slit (see Fig. 1*d*) bisected AR 7563. In Figure 2, the primary target region is in the upper right. In this figure, quiet-Sun areas observed in the SERTS slit (see Fig. 2*d*) are in the center, and NOAA region 7565 is somewhat left of center; additional quiet-Sun structures extend farther to the left. We recognize that an extended loop traverses the area from which we obtain quiet-Sun spectra in pointing position 2; we classify this area as quiet Sun owing to its greatly diminished intensity compared with that of active region 7563. The extended loop appears as bright as it does on the images because we adjusted the contrast to make it more visible.

3.1. *Image Morphology*

It is evident from Figures 1*a*, 1*b* and 2*a*, 2*b* that the *Yohkoh* SXT images and the SERTS Fe XVI and Fe XV images exhibit close structural similarities. Note, in Figure 1, the good correlation between the X-ray and the EUV emission in region 7565 itself, and in the short, narrow loop source directly to its south (both in the far left of the figure). Note, too the extended quiet-Sun loop which stretches from region 7565 into the trailing plage of region 7563, as well as the structures within that trailing plage. Also note the steep drop in intensity with distance from AR 7563 in the direction of the coronal hole to the west. In Figure 2, note the correlation between the X-ray emission and the Fe XVI and XV EUV emission in the loop sources south and east of region 7565. Also note the excellent correspondence between the EUV and X-ray emission in region 7563 and in its trailing plage.

It is evident from Figures 1*c*, 1*d* and 2*c*, 2*d* however, that the SERTS Mg IX and He II images do not manifest the same similarities to the X-ray images that the Fe XVI and XV images do. Although a general correlation with the two active regions is obvious, the following differences are evident. The Mg IX and He II emission generally traces the short, narrow X-ray loop source directly south of region 7565 (as does the Fe XVI and XV emission), but the Mg IX and He II emission in this source increases toward the ends. A likely explanation is that emission from the cooler Mg IX and He II ions is enhanced in the footpoints of this loop and that emission from hotter plasma is enhanced higher up along the loop. Additional, more obvious examples of this are seen in the plage trailing region 7563 (in Figs. 1 and 2), and in the loop sources trailing region 7565. In each case, wherever X-ray sources are nicely traced by Fe XVI and Fe XV emission, only the ends of the sources are seen to be enhanced in Mg IX and He II emission. Furthermore, the quiet-Sun loop which extends from region 7565 to the plage trailing region 7563 is not nicely outlined by either the Mg IX or the He II emission. Finally, neither the Mg IX nor the He II emission diminishes as drastically with distance from region 7563 toward the coronal hole as does the hotter ion emission. In fact, the Mg IX and He II images exhibit some structure in and near the coronal hole, something the Fe XVI, Fe XV, and X-ray images do not.

There is not an exact correspondence between the Mg IX and the He II images, however. Note, for example, several bright areas of Mg IX emission which do not correspond to any particular He II feature: one is evident in Figure 1, just north of the extended loop connecting region 7565 to the plage trailing region 7563; two are evident in Figure 2, one slightly left of the bright portion of 7563 (in an area which appears very dark in X-ray emission), and another below and left of region 7565. In all cases, the areas of enhanced Mg IX emission correspond to regions of low intensity in both the X-ray and the hot EUV lines, but they do not correspond with regions of enhanced He II emission. Nevertheless, because of the proximity of enhanced He II emission sources, one possible interpretation is that *the areas of enhanced* Mg IX *emission correspond to the apexes of cool* ($T \leq 1 \times 10^6$ K) *loops*, and the nearby regions of enhanced He II emission correspond to the loops' footpoints.

Figures 3 (Plate 30) and 4 (Plate 31) show images of photospheric longitudinal magnetograms obtained with the NASA/NSO spectromagnetograph at Kitt Peak National Observatory (Jones et al. 1992). The magnetograms have been rotated forward in time to compensate for the time difference between the acquisition of the magnetograms and the acquisition of the SERTS and *Yohkoh* data. The magnetogram of Figure 3 corresponds to the first SERTS pointing position and that of Figure 4 to the second. The top frame in each figure has Fe XVI intensity contours superposed, and the bottom frame has He II. Note that in both active regions, the most intense Fe XVI and He II emission straddles the neutral line separating regions of opposite magnetic polarity. Outside the active regions, areas of enhanced Fe XVI emission tend to straddle regions of opposite mag-

netic polarity, while areas of enhanced He II emission tend to trace unipolar regions. The latter lends further support to the conclusion that the He II emission tends to outline loop footpoints (which are expected to terminate in regions of opposite magnetic polarity), while the Fe XVI emission tends to outline the higher, hotter portions of the loops. This is consistent with results from *Skylab* observations (e.g., Tousey et al. 1973; Sheeley 1980, 1981; Bray et al. 1991 and references therein).

3.2. *EUV Spectra*

In order to gain insight into the structure and physical processes occurring in active regions and other solar features, it is essential to view those features simultaneously in emission lines which originate in widely differing temperature regimes. The SERTS waveband is well suited to this task, since it includes emission lines formed at temperatures ranging from $\sim 5 \times 10^4$ to $\sim 6 \times 10^6$ K (see Table 1). Unfortunately, this waveband is so densely packed with emission lines that images in most of the available lines are contaminated by overlapping images from nearby spectral lines. Good quality two-dimensional EUV intensity maps are available for only the wavelengths discussed above. However, one-dimensional intensity scans are available for numerous emission lines from the SERTS slit spectra, and we describe them in this section.

The location of the SERTS slit in each pointing position is shown in Figures 1–4. Spectra are available for each of the 64 pixel positions along the slit in each pointing position. Although at least 65 emission lines were observed in the active region spatially averaged spectrum of Brosius et al. (1996), fewer lines are available in the noisier spectra from the individual pixels. Nevertheless, spectral information is available for emission lines which are formed in widely differing temperature regimes, and we present intensity scans for seven such lines in this work. Scans for 15 other lines, not shown here, were also obtained.

Gaussian profiles were fitted to the background-corrected, selected emission lines in the spectrum of each spatial pixel (covering 4.″4116) along the slit. This gave the line centroid wavelengths, integrated intensities, and widths. The line centroid wavelengths were calculated from a wavelength scale which was determined in the laboratory, and the assumption that the He II line in the spatially averaged spectrum is at a wavelength of exactly 303.782 Å. See Brosius et al. (1996) and Thomas & Neupert (1994) for additional details regarding the analysis of SERTS spectral data.

Active region 7563 intensity scans for lines of He II λ303.8, Mg IX λ368.1, Fe XIII λ348.2, Si XI λ303.3, Fe XIV λ334.2, Fe XV λ284.1, and Fe XVI λ335.4 are shown in Figure 5. The final frame of the figure gives a similar scan of the soft X-ray intensity (in DN s^{-1}), taken from the SXT AlMgMn filter image at the location of the SERTS slit. The soft X-ray intensities are indicated by asterisks, with no associated uncertainties. The measured EUV intensity values are indicated by dots, with associated uncertainties as vertical lines. Intensity values were excluded if their uncertainties exceeded 50%, if their line widths were narrower than instrumental, or if the Gaussian fits were deemed unacceptable (e.g., too broad).

Clearly, the active region intensity scans vary substantially with wavelength. For example, features which appear relatively strong in the cool ions, such as the intensity peak between pixels 9 and 18 in the Mg IX (and Fe X λ345.7, not shown here) intensity scan, do not manifest themselves in the intensity scans of the hotter ions. (This peak corresponds to the area of enhanced Mg IX emission just left of the brightest portion of region 7563, seen in Fig. 2) Further, the active region systematically narrows as it is viewed with lines from increasingly hotter ions (except for the He II line, which is optically thick and under investigation in a separate study). We quantified this trend by fitting Gaussian profiles to the intensity scans and calculating the resulting widths (FWHM). Results are shown in Figure 6, where we plot the FWHM (in arcseconds) of the active region intensity as a function of log T_{max}. Asterisks indicate the measured values, and the solid curve is the linear least-squares fit to these values. The dotted line indicates an extrapolation of this curve down to the width of the region as observed in soft X-rays through the AlMgMn broadband filter (the width of the region depends only slightly upon the type of soft X-ray filter used). The corresponding soft X-ray log T_{max} value is 6.51 ± 0.01; we interpret this as an *effective* T_{max} (formation temperature) for the X-ray plasma.

Although we do not show it here, we also obtained an intensity scan of the Ni XVIII (log $T_{max} = 6.52$) line at 320.6 Å, and found detectable emission only in the very core of the active region (pixels 26–43). This core corresponds to the area of strongest soft X-ray emission. We also sought the hotter lines of Fe XVII (log $T_{max} = 6.60$) at 350.5 Å and Ca XVIII (log $T_{max} = 6.76$) at 302.2 Å in this core, but found only the Fe XVII line. Unfortunately, this line was too weak to obtain spatially resolved intensity values; we were able to derive a reliable intensity (34 ergs cm^{-2} s^{-1} sr^{-1}) only for the spatially averaged core spectrum. (Brosius et al. 1996 derived a value of 17 ergs cm^{-2} s^{-1} sr^{-1} from their spectrum which was averaged over a larger portion of the slit.)

Quiet-Sun intensity scans, similar to the active region scans of Figure 5, are shown in Figure 7. It should be pointed out that the eastern end (first four pixels) of the SERTS slit observed sunspot penumbra in NOAA region 7565. This is evident not only as enhanced He II emission in the first four pixels, but also, interestingly, as enhanced Fe XIV and Fe XVI emission in the same pixels. (Fe XV emission, although certainly not diminished in the penumbra, is too noisy for us to make any claims about its enhancement there.) As expected, the soft X-ray emission decreases in the penumbra; this is the only place in the SERTS slit spectra where a noticeable anticorrelation exists between the Fe XVI and the soft X-ray emission.

A maximum in the Mg IX emission occurs at pixels 25–29, and a corresponding enhancement in the noisier Fe X emission (not shown here) occurs at this same location. This corresponds to the area of enhanced Mg IX emission seen just north of the loop connecting region 7565 with the plage trailing region 7563 (see Fig. 1). As was the case with the active region, enhancements in the emission of the cooler lines are not necessarily reflected in the hotter lines. Indeed, a minimum in the soft X-ray, Fe XVI, Fe XV, and Fe XIV emission occurs around pixel 27. This minimum also appears to be visible in Si XI, although it is shifted somewhat westward (toward higher pixel numbers).

3.3. *Temperature*

We followed the method of Brosius et al. (1996) to obtain the logarithmic temperature scans shown in Figure 8 from the representative line intensity ratios of Fe XVI λ335.4/Fe XIV λ334.2 and Fe XVI λ335.4/Fe XV

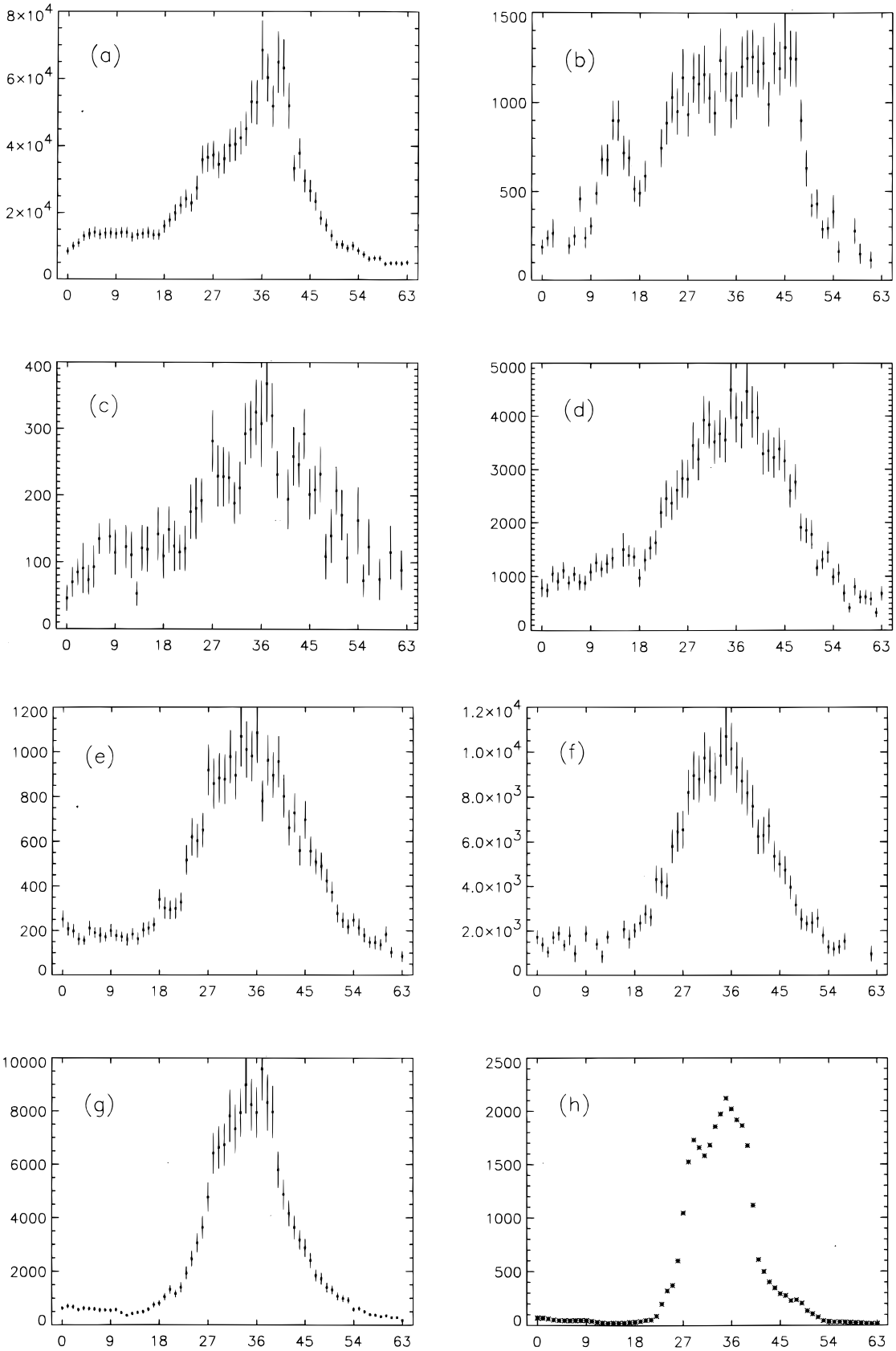

FIG. 5.—Slit intensity scans for (*a*) He II λ303.8, (*b*) Mg IX λ368.1, (*c*) Fe XIII λ348.2, (*d*) Si XI λ303.3, (*e*) Fe XIV λ334.2, (*f*) Fe XV λ284.1, (*g*) Fe XVI λ335.4, and (*h*) soft X-rays through the *Yohkoh* SXT AlMgMn filter, obtained in the first SERTS pointing position. In this position, the SERTS slit bisected region 7563. EUV intensities are in ergs cm^{-2} s^{-1} sr^{-1}, and X-ray intensities are in DN s^{-1}.

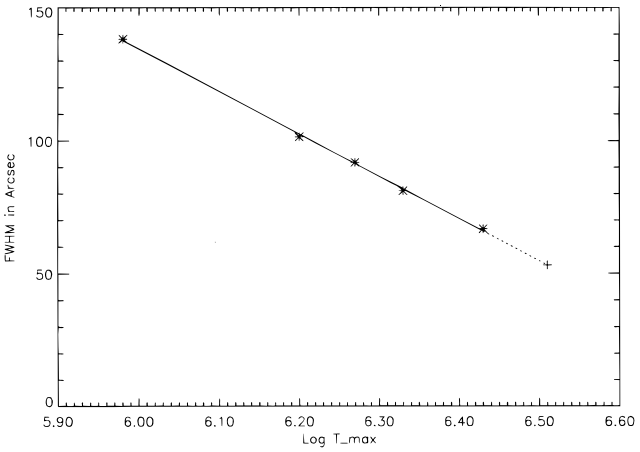

FIG. 6.—Plot of active region 7563 width (FWHM), derived from emission-line intensity scans along the SERTS slit, vs. log T_{max} of the lines. The solid curve shows a linear fit to the measured values (*asterisks*), and the dotted curve shows an extrapolation to the measured soft X-ray width (*cross*). This extrapolation indicates that the effective log T_{max} for the soft X-rays is 6.51, in agreement with other results described in the text.

λ284.1. Based upon the measurement uncertainties, the derived temperatures exhibit *significant but not substantial* systematic variations across the slit in both pointing positions. In position 1 (Figs. 8*a*, 8*b*), the temperature increases from the outskirts toward the core of the active region (by ~0.15 dex for Fe XVI/Fe XV, and ~0.08 dex for Fe XVI/Fe XIV). In position 2 (Figs. 8*c*, 8*d*), the temperature is highest in the sunspot pixels (0–3) and decreases toward a minimum around pixel 27 (where the Fe XIV, XV, XVI and soft X-ray intensities are minimized, and the Mg IX intensity is maximized). Averaged over the active region pixels (16–52), the Fe XVI/Fe XV and Fe XVI/Fe XIV ratios yield temperature logarithms of 6.39 ± 0.04 and 6.32 ± 0.02; averaged over the quiet Sun, these same line ratios yield values of 6.31 ± 0.04 and 6.27 ± 0.02. Thus the active region and quiet-Sun temperature values derived from these line intensity ratios differ, but not greatly. Cheng (1980) found a similar result: using Fe XVI and Fe XV images obtained from *Skylab*, he derived nearly equal temperatures in distinct active region loops and in their surrounding structures.

Similar temperature scans, not shown here, were constructed from the ratios of Fe XIII λ348.2/Fe XII λ352.1 and Fe XII λ352.1/Fe X λ345.7. These plots show more scatter than those of Figure 8, but no systematic trends are evident: the derived temperature remains constant (within the uncertainties) across the slit. This supports the conclusion of Brosius et al. (1996) that temperatures derived from intensity ratios among lines of only Fe X, XI, XII, and XIII are not significantly different in the active region than in the quiet Sun. Indeed, averaged over the active region pixels, the Fe XIII/Fe XII and Fe XII/Fe X ratios yield temperature logarithms of 6.14 ± 0.04 and 6.07 ± 0.02; averaged over the quiet Sun, these same line ratios yield values of 6.15 ± 0.06 and 6.06 ± 0.04.

Maps of the active region temperature were derived from three different SXT filter ratios: AlMgMn/thick Al, thin Al/thick Al, and thin Al/AlMgMn. All maps were derived from composite images of multiple duration exposures obtained in the partial frame imaging (PFI, pixel size = 2.″455) mode. A map of the quiet-Sun temperature was derived from only the thin Al/AlMgMn SXT filter ratio. This map was derived from composite images of multiple duration exposures obtained in the full frame imaging (FFI, pixel size = 4.″910) mode. In addition, active region and quiet-Sun temperature maps were derived from ratios of the SERTS images of Fe XVI λ335.4 to Fe XV λ284.1. Since (i) these maps show relatively little temperature variation across the regions and (ii) the SERTS slit spectral data provide wider and more reliable temperature diagnostic capabilities than the SERTS images, we restrict our treatment of temperature diagnostics in this paper to the area covered by the SERTS slit.

Figure 9 shows the active region and quiet-Sun temperature scans derived from the *Yohkoh* SXT filter ratios listed above for the locations of the SERTS slit. The temperature scans in this figure correspond to those in Figure 8. The highest X-ray temperatures were derived from the AlMgMn/thick Al filter ratio (Fig. 9*c*); however, the differences between the AlMgMn/thick Al and the thin Al/thick Al temperatures may not be statistically significant, judging from the uncertainties. Averaged over the active region pixels (16–52), the corresponding log T values are 6.49 ± 0.03 and 6.45 ± 0.02. The temperature derived from the AlMgMn/thin Al filter ratio is systematically lower than that derived from the other two filter ratios, a result which is consistent with the conclusions of Hara et al. (1992). We obtain log $T = 6.33 \pm 0.03$ averaged over the active region pixels, a value which is intermediate to those derived from the Fe XVI λ335.4/Fe XV λ284.1 and Fe XVI λ335.4/Fe XIV λ334.2 line intensity ratios from SERTS. For the quiet Sun, the temperature derived from the AlMgMn/thin Al filter is lower than that derived from the Fe XVI λ335.4/Fe XIV λ334.1 ratio. This further indicates, as Hara et al. (1992) concluded, that the AlMgMn/thin Al filter ratio is not typically sensitive to the hottest plasma along the line of sight.

As mentioned earlier, emission in the Ca XVIII λ302.2 line (log $T_{max} = 6.76$) was sought but not detected in the active region core. While this nondetection does not rule out the presence of plasma with log $T_{max} \sim 6.76$, it certainly demonstrates that such plasma is present in such low quantities as to be undetectable via emission lines. Plasma with log $T \sim 6.76$ was also not detected by *Yohkoh*, since the maximum active region temperature logarithm derived from filter ratios was 6.62 ± 0.04 (see Fig. 9). It sould be pointed out that the DEM curve of Brosius et al. (1996) suggests that plasma with log T as high as 7.0 is present in the active region; however, the curve reaches its maximum at log $T \sim 6.2$, and drops sharply for log $T > 6.65$. Uncertainties on the high-temperature portion of the DEM distribution are quite large owing to the absence of emission lines with which to fit the curve in that temperature range. The presence of high-temperature (log $T > 6.7$) plasma in the DEM curve was derived only from the intensities of cooler lines.

Also as mentioned earlier, emission in the Fe XVII λ350.5 line (log $T_{max} = 6.60$) was detected in the active region core (pixels 26–43). From the ratio of the averaged Fe XVII to Fe XVI core emission, we obtain log $T = 6.64 \pm 0.05$. This is higher than both the average (log $T = 6.57 \pm 0.03$) and the maximum (6.62 ± 0.04) core temperatures derived from the SXT AlMgMn/thick Al filter ratio, but the differences are not statistically significant in light of the uncertainties. Finally, the soft X-ray "effective T_{max}" inferred from the slit intensity scan measurements (6.51 ± 0.01) is consistent

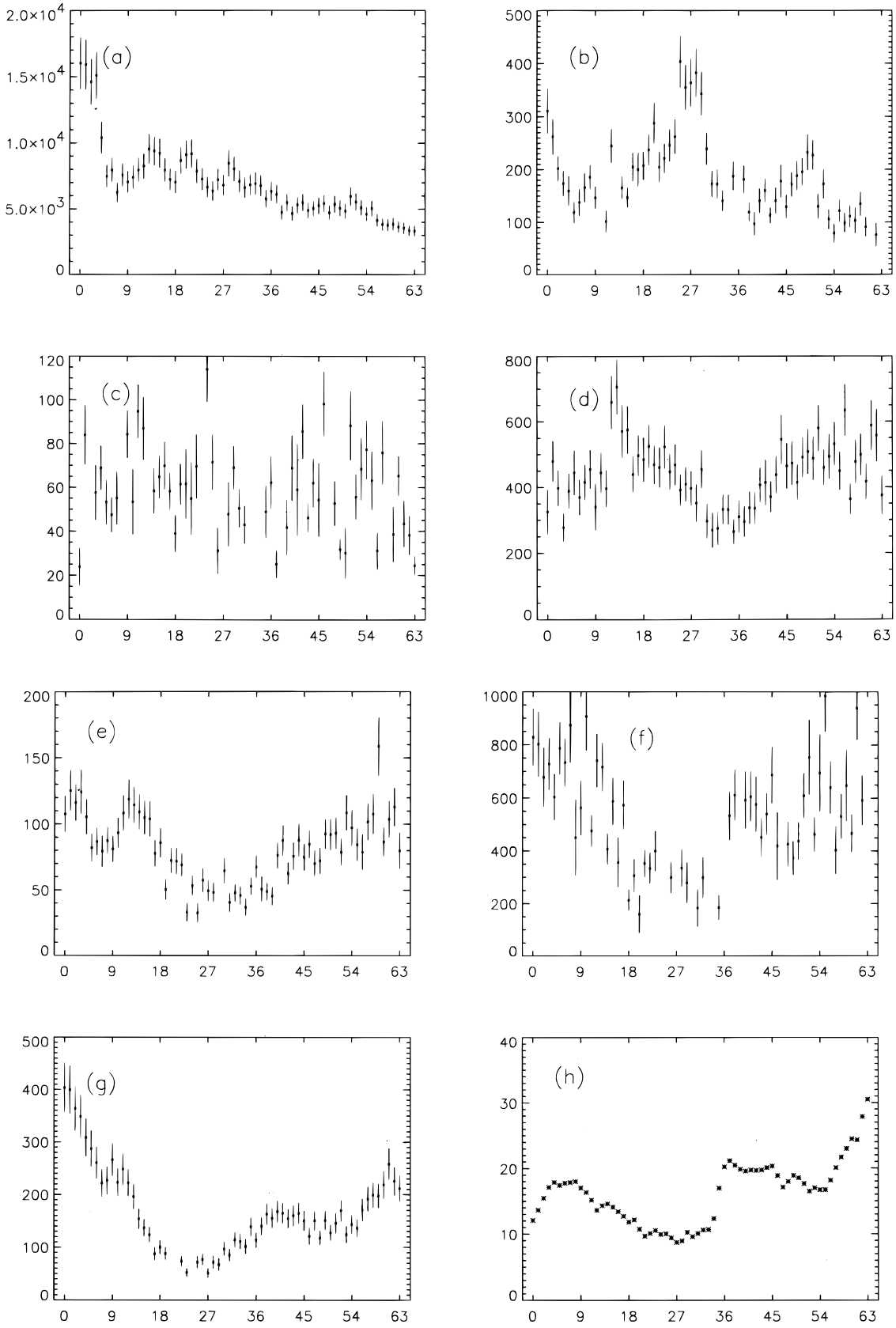

FIG. 7.—Slit intensity scans for the same lines as in Fig. 5, obtained in SERTS pointing position 2 (quiet Sun)

(within $\pm$ 0.1 dex) with the temperature logarithms derived from the SXT AlMgMn/thick Al and thin Al/thick Al filter ratios. We conclude that all of the methods employed above to infer or derive coronal plasma temperatures are mutually consistent, and that the coordinated SERTS and *Yohkoh* observations provide a greater range in spatially resolvable temperature coverage than that available to either instrument alone.

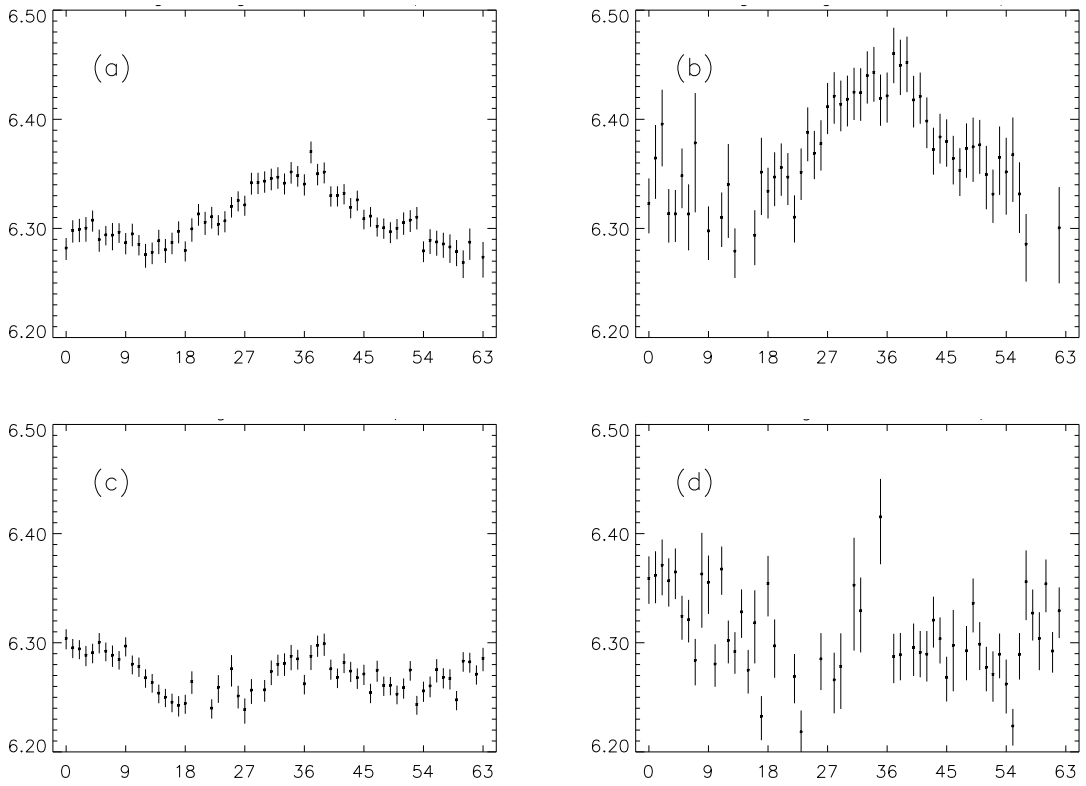

FIG. 8.—Active region temperature scans derived from line ratios of (*a*) Fe XVI λ335.4/Fe XIV λ334.2 and (*b*) Fe XVI λ335.4/Fe XV λ284.1. Quiet-Sun temperature scans derived from (*c*) Fe XVI λ335.4/Fe XIV λ334.2 and (*d*) Fe XVI λ335.4/Fe XV λ284.1.

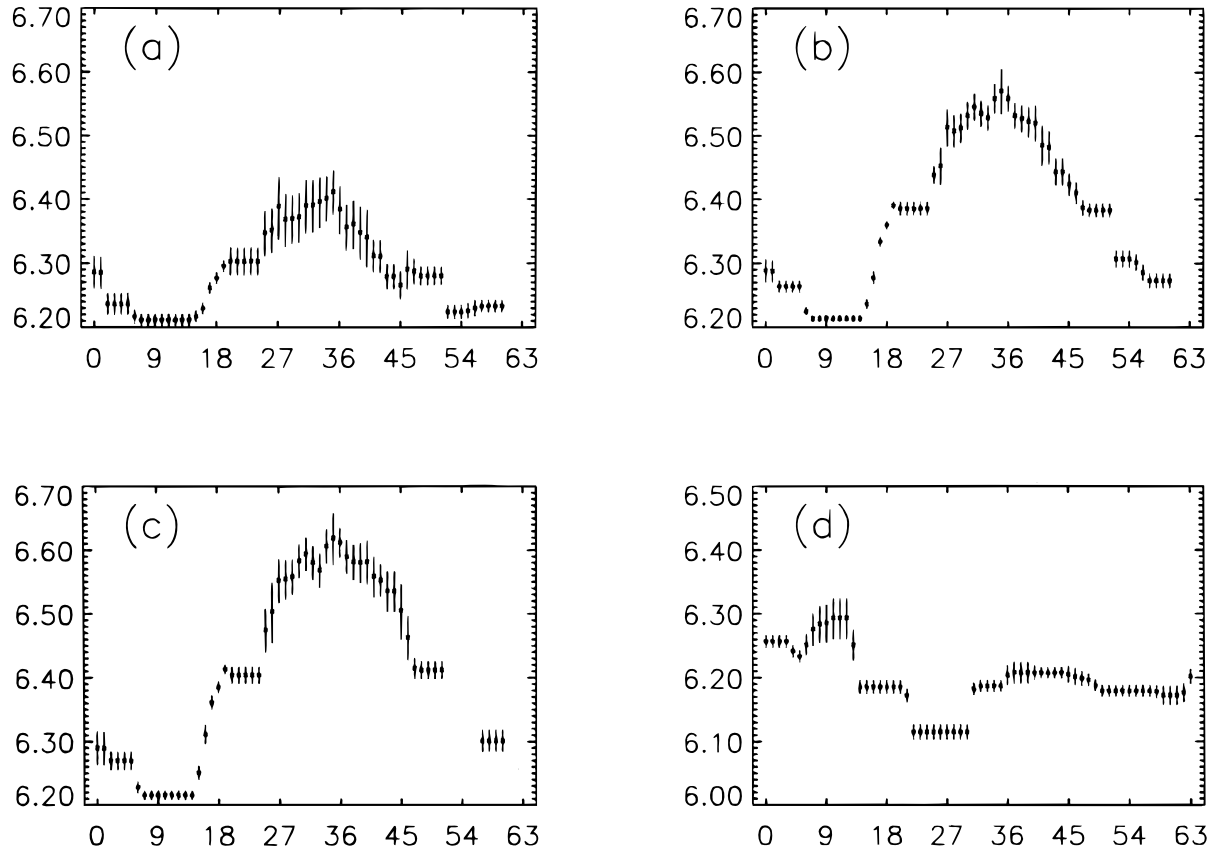

FIG. 9.—Active region temperature scans derived from *Yohkoh* SXT filter ratios: (*a*) AlMgMn/thin Al, (*b*) thick Al/thin Al, and (*c*) thick Al/AlMgMn. (*d*) Quiet-Sun temperature scan derived from SXT AlMgMn/thin Al filter ratio.

3.4. *Density*

Brosius et al. (1996) calculated active region and quiet-Sun densities with numerous iron line intensity ratios derived from spatially averaged SERTS slit spectra. Here we present results for two of their ratios which are best for analysis with our spatially resolved spectra: Fe XIV λ353.9/λ334.2, and Fe XIII λ359.7/λ348.2. Throughout this work, "density" is understood to mean the density of the emitting plasma, which may fill only a fraction f of the total volume along the line of sight. We followed the method of Brosius et al. (1996), and used the line emissivity tables provided therein, to obtain the active region and quiet-Sun logarithmic density scans shown in Figure 10. This figure reveals that for each of these density sensitive line ratios, *the density does not vary significantly or systematically across the SERTS slit in either pointing position, despite the fact that the emission-line intensities themselves very substantially*. Let us consider the physical implications of this observed density invariance on active region structures.

The intensity of an emission line can be written

$$I = \frac{1}{4\pi} \int fP \, dl \, , \tag{1}$$

where P is the power emitted per unit volume, dl is the path length along which the emission originates, and f is the filling factor, i.e., the fraction of the observed volume from which the observed radiation actually emanates. Assuming for simplicity that the density and temperature are constant over the emitting region of dimension Δl, equation (1) can be rewritten

$$I = \frac{1}{4\pi} f \left(\frac{P}{n_e n_{\rm H}} \right) n_e n_{\rm H} \Delta l \, , \tag{2}$$

where $P/n_e n_{\rm H} = \rho$ is the line emissivity, a function of density and temperature. With the usual assumption that $n_{\rm H} = 0.8 n_e$, the line intensity can be written as

$$I = \frac{0.8 n_e^2 \rho f \Delta l}{4\pi} \, . \tag{3}$$

The ratio of line intensities from two different areas on the Sun (area 1 and area 2) is then given by

$$\frac{I_1}{I_2} = \frac{[n_e^2 \rho f \Delta l]_1}{[n_e^2 \rho f \Delta l]_2} \, . \tag{4}$$

Let areas 1 and 2 correspond to locations along the SERTS slit in region 7563 (Figs. 10*a*, 10*b*). Since the densities are equal (within the measurement uncertainties) for such positions, the density is explicitly eliminated from equation (4). Further, under the reasonable assumption that the emission for any given line originates in plasma at the appropriate $T_{\rm max}$ value (the formation temperature), the emissivities ρ_1 and ρ_2 are also equal and therefore eliminated from equation (4). This leaves

$$\frac{I_1}{I_2} = \frac{[f \Delta l]_1}{[f \Delta l]_2} \, , \tag{5}$$

which means that *the intensity variations through the active region are due to variations in $f\Delta l$, not to variations in density*. Since the emission-line intensities increase toward the center of the active region (see Fig. 5), the product of the path length and the volume filling factor must also increase toward the center of the active region. From Figure 5*c*, we estimate the intensity ratio of Fe XIII from the active region core to the active region outskirts to be $\sim$3. This means that, for Fe XIII emission, $[f\Delta l]_{\rm core} \sim 3[f\Delta l]_{\rm outskirts}$. Similarly, for Fe XIV emission (Fig. 5*e*), $[f\Delta l]_{\rm core} \sim 5[f\Delta l]_{\rm outskirts}$.

It is interesting to note that the active region and quiet-Sun densities differ by factors of only about 2: Brosius et al (1996) obtained averaged active region and quiet-Sun density logarithms of 9.58 ± 0.14 and 9.35 ± 0.11 for Fe XIV, and 9.26 ± 0.10 and 8.93 ± 0.15 for Fe XIII. We therefore interpret the observed intensity differences between the active region and quiet-Sun as follows. From the spatially averaged active region and quiet-Sun intensities tabulated in Brosius et al. (1996), the active region to quiet-Sun intensity ratios for Fe XIV λ334 and Fe XIII λ348 are $R_{334} = 8.15$ and $R_{348} = 3.82$. (The intensity ratios can also be estimated from the plots in Fig. 5 and 7 of this paper.) Rearranging equation (4), inserting R for $I_{\rm ar}/I_{\rm qs}$, and substituting χ for $[f\Delta l]_{\rm ar}/[f\Delta l]_{\rm qs}$, we obtain

$$\chi = R \, \frac{[n_e^2 \rho]_{\rm qs}}{[n_e^2 \rho]_{\rm ar}} \, . \tag{6}$$

With the measured values for R and n_e given above, and with interpolated values for the emissivities ρ (evaluated at $T = T_{\rm max}$ and the appropriate measured electron densities, from Appendix A of Brosius et al. 1996), we obtain $\chi_{334} = 3.1$ and $\chi_{348} = 1.1$. This tells us that $[f\Delta l]_{\rm ar} = [f\Delta l]_{\rm qs}$ for Fe XIII, which means that *on average, the density difference accounts for the* Fe XIII *intensity difference between the active region and quiet-Sun.* (A similar result holds for Fe XII emission lines as well.) For Fe XIV, however, $[f\Delta l]_{\rm ar} = 3[f\Delta l]_{\rm qs}$, which means that the measured density difference alone is *not* sufficient to account for the observed intensity difference. *For* Fe XIV *the product of the path length and the volume filling factor must be greater in the active region than in the quiet Sun.*

It would be interesting to extend the above analyses to emission lines of Fe XV and XVI, which show greater intensity variations across region 7563 as well as greater active region over quiet-Sun intensity enhancements than the lines from the ions treated above. Unfortunately, the density-sensitive line ratio measurements which are needed in order to carry out the procedure are not available. It should be pointed out, however, that active region over quiet-Sun density enhancements by factors of $\sim$2 would *not* be sufficient to explain the observed active region over quiet-Sun intensity enhancements: significant enhancements in $f\Delta l$ would also be required.

3.5. *Doppler Shifts*

The centroid of each emission line that we analyzed in the spatially resolved SERTS slit spectra shifted with position along the slit. These shifts could be manifestations of real mass motions, but without an absolute (as opposed to relative) wavelength scale against which to compare them, such a conclusion cannot be immediately substantiated. In order to ascertain the viability of the mass motion explanation for the apparent Doppler shifts in the EUV lines, we derived lower limits on statistically significant wavelength shifts by the following method.

As mentioned above, SERTS obtained four different exposures in each of two different pointing positions in order to ensure the availability of optimally exposed spectra

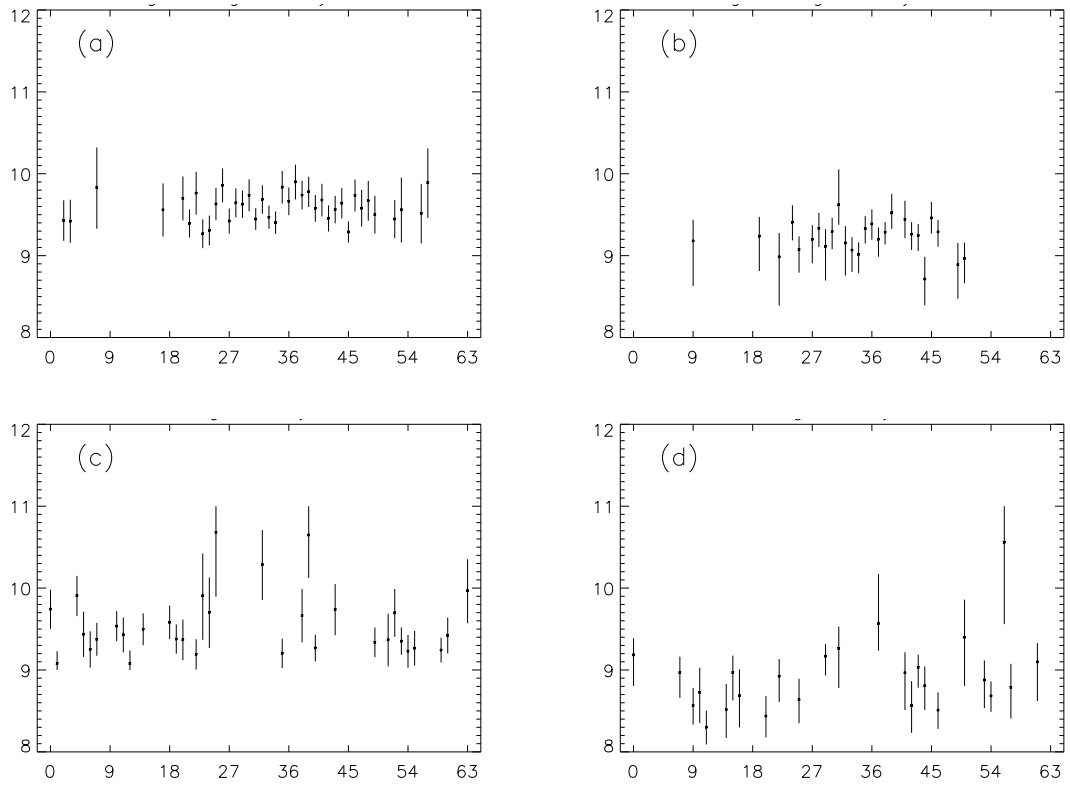

FIG. 10.—Active region density scans derived from (*a*) Fe XIV λ353.9/λ334.2 and (*b*) Fe XIII λ359.7/λ348.2. Quiet-Sun density scans derived from (*c*) Fe XIV λ353.9/λ334.2 and (*d*) Fe XIII λ359.7/λ348.2.

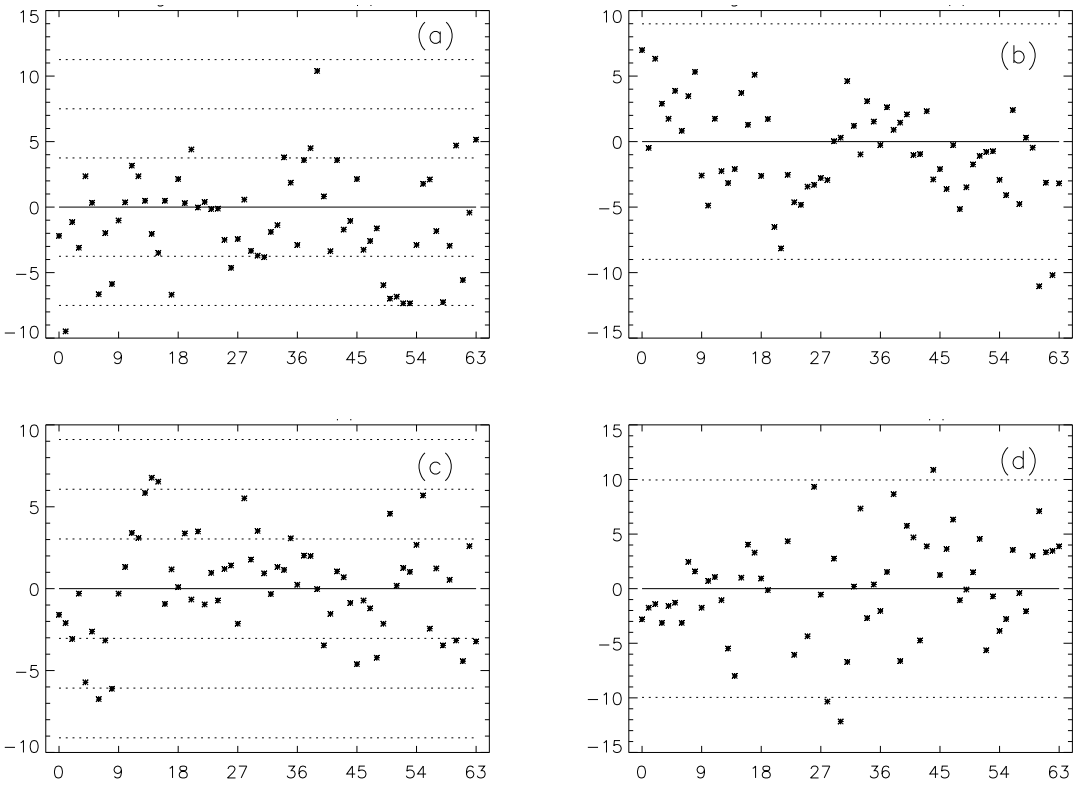

FIG. 11.—Doppler shifts in km s^{-1} for selected EUV lines. (*a*) He II λ303.8 in region 7563, (*b*) Fe XVI λ335.4 in region 7563, (*c*) He II λ303.8 in the quiet Sun, and (*d*) Fe XVI λ335.4 in the quiet Sun. Negative values correspond to blueshifts, and positive values to redshifts. The solid horizontal line indicates a zero shift for reference. The dotted horizontal lines in the plot for He II indicate ± 1, 2, and 3 σ. The dotted horizontal lines in the Fe XVI plots indicate the lower limits on significant detections ($\pm \Delta V_{\rm min}$, as described in the text). We do not obtain statistically significant detections of mass motions in either active region 7563 or in the quiet Sun.

and images for emission lines of widely varying intensities. In this work, the longest two exposures in each pointing position were the most useful: we used spatially averaged spectra derived from them (e.g., Brosius et al. 1996) to determine two values of the centroid wavelength of every line in each pointing position. The differences provide estimates of the repeatability of line wavelength measurements. We also included observations from the 1991 SERTS flight in this process. For each wavelength, we adopted the *largest* differences as our estimate of the measurement repeatability uncertainty. Since the individual pixel spectra are noisier than the spatially averaged spectra from which the wavelength repeatability uncertainty was derived above, we also obtained the standard deviation of the wavelength shifts for each wavelength in each (active region and quiet-Sun) spatially resolved spectrum. For each line in each spectrum, we took the sum of the repeatability uncertainty and the standard deviation as a lower limit for reliable detections of Doppler shifts due to mass motions ($\Delta V_{\rm min}$). (For every spectrum in every pointing position, the relative wavelength scale was fixed so that the wavelength of the strong He II line in the spatially averaged spectrum was at a wavelength of exactly 303.782 Å.)

Figure 11 shows the measured wavelength shifts for He II λ303.8 and Fe XVI λ335.4, in km s^{-1}, along the SERTS slit in pointing positions 1 (active region) and 2 (quiet Sun). Negative values correspond to upflows, and positive to downflows. The solid horizontal line in each frame shows a zero shift for reference. For Fe XVI λ335.4, the horizontal dotted lines indicate $\pm \Delta V_{\rm min}$. For the He II line, no repeatability uncertainty measurements were available since this line's wavelength was *defined* to be exactly 303.782 Å in each spatially averaged spectrum; the horizontal dotted lines in the He II frames indicate ± 1, 2, and 3 σ. It is evident from Figure 11 that wavelength shifts in the He II and Fe XVI lines are quite small ($\lesssim$10 km s^{-1}), and do not provide statistically significant detections of Doppler shifts due to mass motions. A similar analysis of the Mg IX λ368, Fe XIII λ348, Si XI λ303, Fe XIV λ334, and Fe XV λ284 lines yields the same conclusion: *we do not detect Doppler shifts due to mass motions in the EUV emission lines in either the active region or the quiet Sun.*

4. CONCLUSIONS

Following is a summary of our conclusions from this work.

1. The SERTS images in Fe XV and XVI exhibit remarkable morphological similarity to the *Yohkoh* SXT images: the EUV emission from these hot ions generally outlines the same loop structures seen in soft X-rays. EUV emission from the cooler He II and Mg IX ions, although closely associated with the soft X-ray structures, tends to delineate loop footpoints as well as structures which are not necessarily associated with the hot loops. These structures may be cool ($T \lesssim 1 \times 10^6$ K) loops.

2. From the spatially resolved SERTS slit spectra, we obtained one-dimensional intensity scans for emission lines of He II, Mg IX, Fe XIII, Si XI, Fe XIV, Fe XV, and Fe XVI. These scans show that active region 7563 systematically narrows as it is viewed with successively hotter lines, and it appears narrowest in the broadband soft X-ray emission. The active region width (full width at half-maximum intensity) diminishes linearly with log $T_{\rm max}$. The linear fit to this width yields an extrapolated effective log $T_{\rm max}$ of 6.51 ± 0.01 for the soft X-ray emission.

3. Active region and quiet-Sun one-dimensional temperature scans were derived from intensity ratios of spatially resolved slit spectral lines, and from coregistered SXT filter ratios. The highest plasma temperatures were measured in the most intense, central core of region 7563. The temperatures derived from Fe XVI λ335.4/Fe XV λ284.1 and Fe XVI λ335.4/Fe XIV λ334.2 exhibit significant (based upon the measurement uncertainties) but not substantial ($\sim$0.15 and $\sim$0.08 dex, respectively) variations across the SERTS slit in both pointing positions; in particular, they systematically increase toward the interior of region 7563 and in the sunspot penumbra of region 7565. Somewhat larger systematic variations were obtained from all available SXT filter ratios. The Fe XIII λ348.2/Fe XII λ352.1 and Fe XII λ352.1/Fe X λ345.7 ratios show more temperature scatter, but the systematic trends seen in the hotter ion ratios are absent; these line ratios yield the same temperature both inside and outside the active regions. Temperatures derived from SXT filter ratios and from the SERTS line intensity ratios, although not equal, are mutually consistent.

4. The electron density does not vary significantly or systematically across the SERTS slit in either pointing position, despite the fact that the emission line intensities themselves vary substantially across the same areas on the Sun. This was used to show that the product of the volume filling factor and the path length must be greater in the active region core than in the active region outskirts. From the Fe XIII line intensities we found $[f\Delta l]_{\rm core} \sim 3[f\Delta l]_{\rm outskirts}$, and from Fe XIV we found $[f\Delta l]_{\rm core} \sim 5[f\Delta l]_{\rm outskirts}$. Density sensitive line intensity ratios of Fe XII, XIII, and XIV indicate that the active region densities are $\sim$2 times the quiet-Sun densities. For the Fe XII and XIII lines, this density enhancement is sufficient to account for the observed active region over quiet-Sun intensity enhancement. For the Fe XIV lines, the active region over quiet-Sun intensity enhancement can be explained only by an additional enhancement in the product of the filling factor and the path length: $[f\Delta l]_{\rm ar} = 3[f\Delta l]_{\rm qs}$.

5. None of the SERTS emission lines exhibited significant Doppler shifts in either NOAA region 7563 or in the quiet Sun.

J. W. B. acknowledges NASA support through contracts NASW-4933 and NASW-5020. J. M. D. and R. J. T. acknowledge NASA support for the SERTS program through RTOP grants 879-11-38 and 170-38-52. NSO/Kitt Peak data used here are produced cooperatively by NSF/NOAO, NASA/GSFC, and NOAA/SEL. B. C. M. F. acknowledges support from the Italian Space Agency (ASI).

REFERENCES

Arnaud, M., & Raymond, J. 1992, ApJ, 398, 394
Behring, W. E., Cohen, L., Feldman, U., & Doschek, G. A. 1976, ApJ, 203, 521
Bray, R. J., Cram, L. E., Durrant, C. J., & Loughhead, R. E. 1991, Plasma Loops in the Solar Corona (Cambridge: Cambridge Univ. Press)
Brosius, J. W., Davila, J. M., Thomas, R. J., & Monsignori-Fossi, B. C. 1996, ApJS, 106, 143
Brosius, J. W., Davila, J. M., Thomas, R. J., & Thompson, W. T. 1994, ApJ, 425, 343
Brosius, J. W., et al. 1993, ApJ, 411, 410

Brosius, J. W., Willson, R. F., Holman, G. D., & Schmelz, J. T. 1992, ApJ, 386, 347
Cheng, C.-C. 1980, ApJ, 238, 743
Davila, J. M., Thomas, R. J., Thompson, W. T., Keski-Kuha, R. A. M., & Neupert, W. M. 1993, in UV and X-Ray Spectroscopy of Laboratory and Astrophysical Plasma, ed. E. Silver & S. Kahn (Cambridge: Cambridge Univ. Press), 301
Dere, K. P. 1978, ApJ, 221, 1062
Dere, K. P., Mason, H. E., Widing, K. G., & Bhatia, A. K. 1979, ApJS, 40, 341
Dupree, A. K., Huber, M. C. E., Noyes, R. W., Parkinson, W. H., Reeves, E. M., & Withbroe, G. L. 1973, ApJ, 182, 321
Falconer, D. A. 1994, Ph.D. thesis, Univ. Maryland
Gerassimenko, M., Solodyna, C. V., & Nolte, J. T. 1978, Sol. Phys., 57, 103
Hara, H., Tsuneta, S., Lemen, J. R., Acton, L. W., & McTiernan, J. M. 1992, PASJ, 44, L135
Harvey, J. W., & Sheeley, N. R. 1977, Sol. Phys., 54, 343
Jones, H. P., Duvall, T. L., Jr., Harvey, J. W., Mahaffey, C. T., Schwitters, J. D., & Simmons, J. E. 1992, Sol. Phys., 139, 211
Jordan, S. D., Thompson, W. T., Thomas, R. J., & Neupert, W. M. 1993, ApJ, 406, 346
Keski-Kuha, R. A. M., Thomas, R. J., & Davila, J. M. 1992, Proc. SPIE, 1546, 614
Monsignori-Fossi, B. C. 1992, unpublished
Neupert, W. M., Brosius, J. W., Thomas, R. J., & Thompson, W. T. 1992a, ApJ, 392, L95
Neupert, W. M., Epstein, G. L., Thomas, R. J., & Thompson, W. T. 1992b, Sol. Phys., 137, 87
Neupert, W. M., Thomas, R. J., & Chapman, R. D. 1974, Sol. Phys., 34, 349
Nitta, N., et al. 1991, ApJ, 374, 374
Pye, J. P., Evans, K. D., Hutcheon, R. J., Gerassimenko, M., Davis, J. M., Krieger, A. S., & Vesecky, J. F. 1978, A&A, 65, 123
Saba, J. L. R., & Strong, K. T. 1991, ApJ, 375, 789
Schmelz, J. T., Holman, G. D., Brosius, J. W., & Gonzales, R. D. 1992, ApJ, 399, 733
Schmelz, J. T., Holman, G. D., Brosius, J. W., & Willson, R. F. 1994, ApJ, 434, 786
Sheeley, N. R. 1980, Sol. Phys., 66, 79
———. 1981, in Solar Active Regions, ed. F. Q. Orrall (Boulder: Colorado Associated University Press), 32
Thomas, R. J., Keski-Kuha, R. A. M., Neupert, W. M., Condor, C. E., & Gum, J. S. 1991, Appl. Opt., 30, 2245
Thomas, R. J., & Neupert, W. M. 1994, ApJS, 91, 461
Thompson, W. T., Neupert, W. M., Jordan, S. D., Jones, H. P., Thomas, R. J., & Schmieder, B. 1993, Sol. Phys., 147, 29
Tousey, R., et al. 1973, Sol. Phys., 33, 265
Tousey, R., Bartoe, J.-D. F., Brueckner, G. E., & Purcell, J. D. 1977, Appl. Opt., 16, 870
Tsuneta, S., et al. 1991, Sol. Phys., 136, 37
Vaiana, G. S., Krieger, A. S., & Timothy, A. F. 1973, Sol. Phys., 32, 81
Vernazza, J. E., & Reeves, E. M. 1978, ApJS, 37, 485
Webb, D. F. 1981, in Solar Active Regions, ed. F. Q. Orrall (Boulder: Colorado Associated Univ.), 165
Webb, D. F., Holman, G. D., Davis, J. M., Kundu, M. R., & Shevgaonkar, R. K. 1987, ApJ, 315, 716

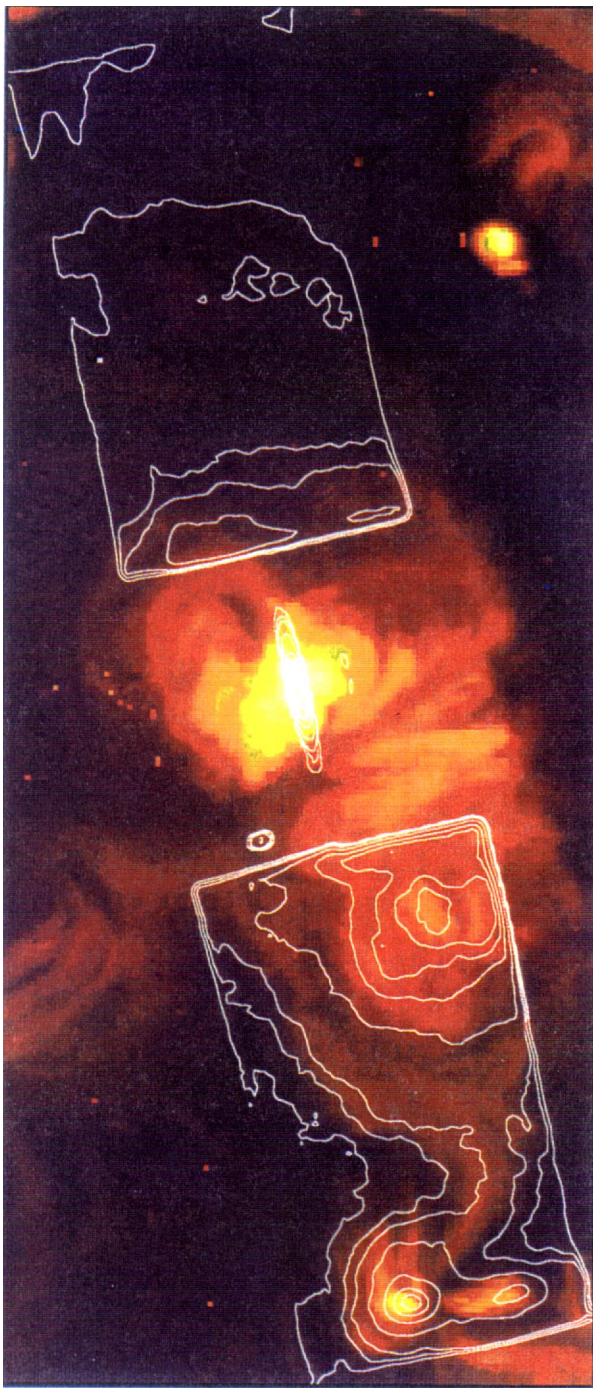

FIG. 1*a*

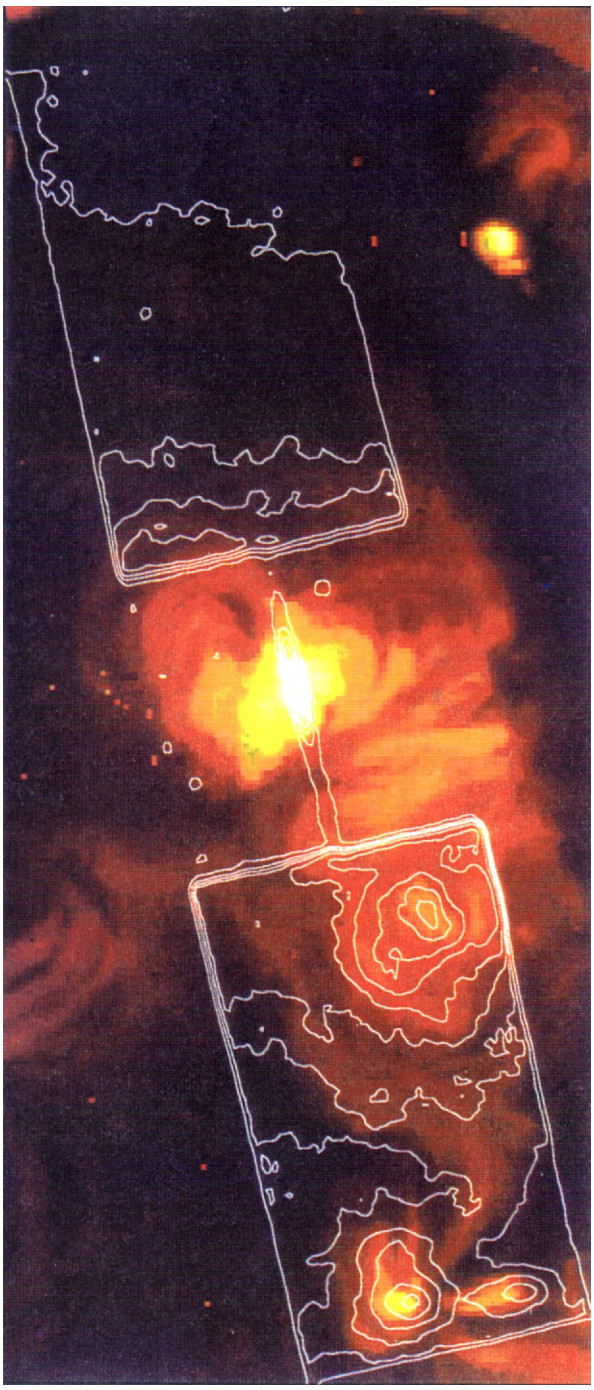

FIG. 1*b*

FIG. 1.—The color image in each frame is a composite image of three SXT exposures through the AlMgMn filter, corresponding to SERTS pointing position 1. The area covered is 1293 × 560 arcsec^2. SERTS intensity contours in lines of (*a*) Fe XVI λ335.4, (*b*) Fe XV λ284.1, (*c*) Mg IX λ368.1, and (*d*) He II λ303.8 are superimposed. Intensity contours in ergs cm^{-2} s^{-1} sr^{-1} are (*a*) 50, 75, 100, 200, 400, 600, 800, 1000; (*b*) 280, 400, 500, 600, 800, 1200, 1600, 2000, 2300; (*c*) 100, 150, 200, 250, 300, 350; (*d*) 4000, 6000, 8000, 12000, 15000. The lobe-slit-lobe format of the SERTS data is evident, although the intensity contours in the slit portion of these figures should not be taken seriously. The location of the SERTS slit, from which the spatially resolved spectra used in this paper were obtained, is shown in the last frame. NOAA region 7563 is in the center of each frame in this figure, and the coronal hole is toward the right. Region 7565 is the brightest area in the far left.

BROSIUS et al. (see 477, 971)

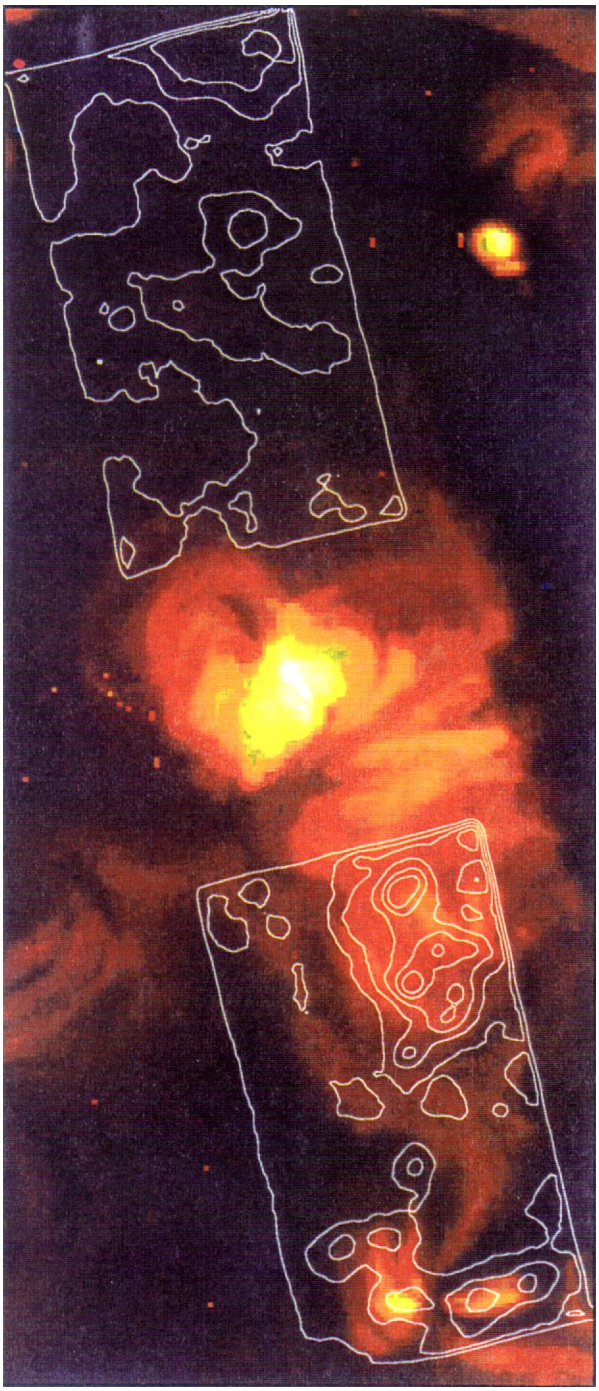

FIG. 1*c*

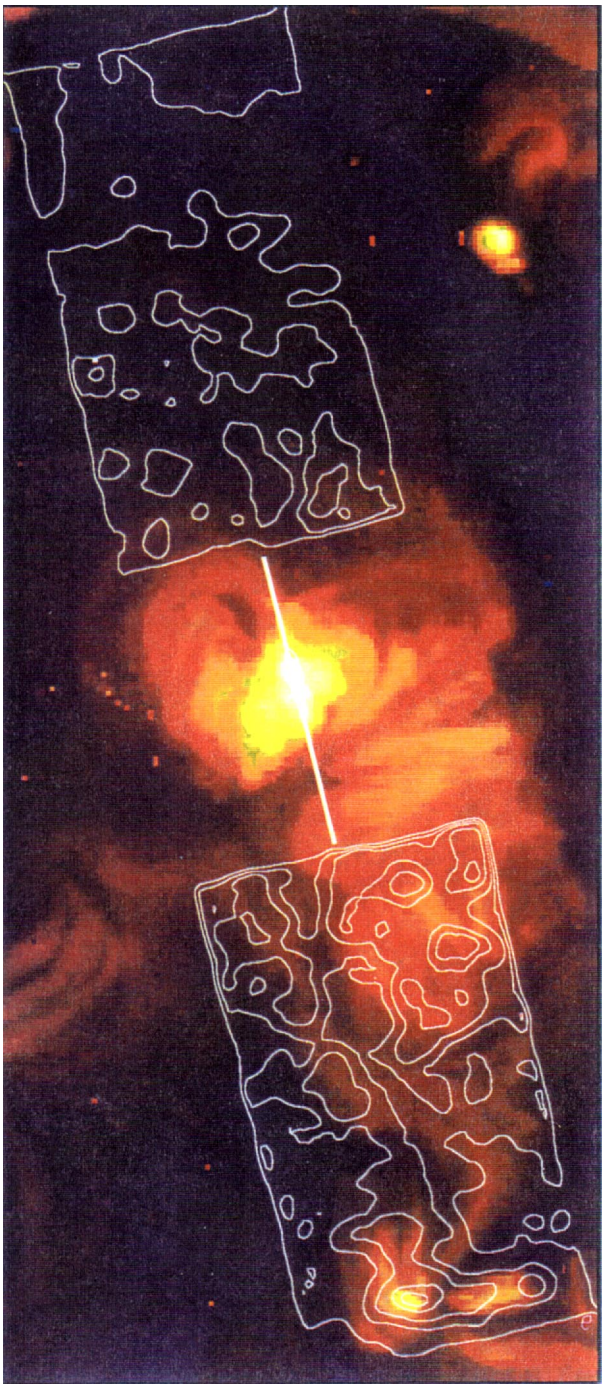

FIG. 1*d*

BROSIUS et al. (see 477, 971)

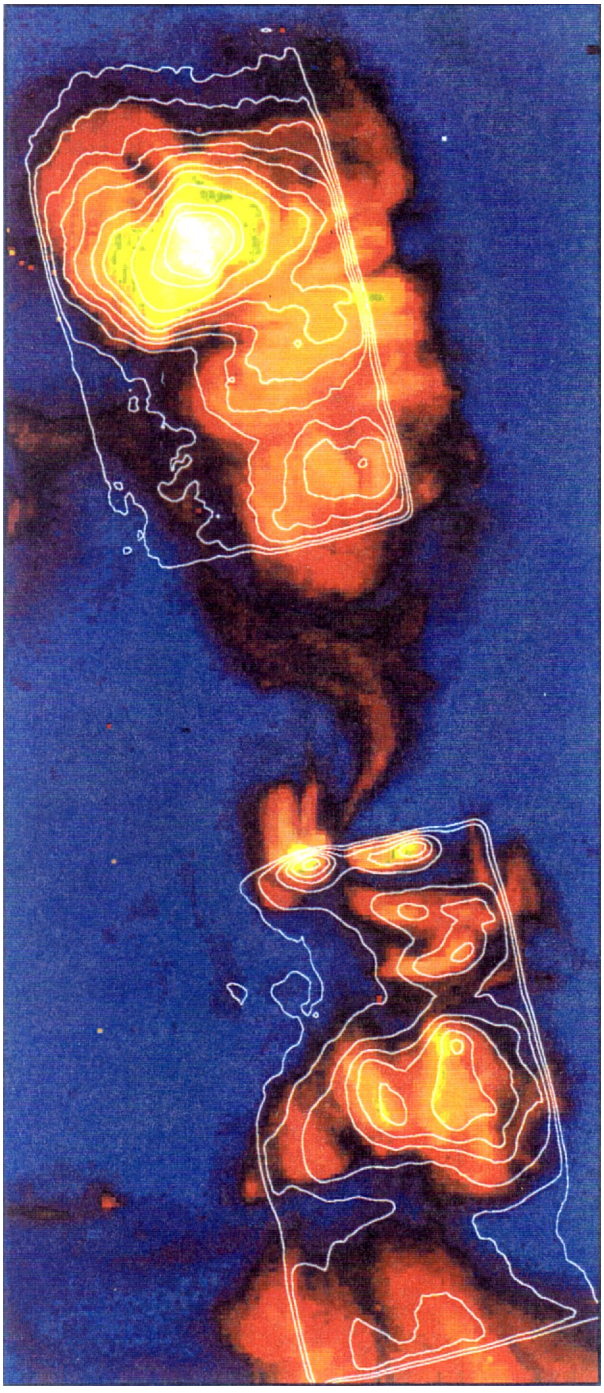

FIG. 2*a*

FIG. 2*b*

FIG. 2.—The color image in each frame is a composite image of three *Yohkoh* SXT exposures through the AlMgMn filter, corresponding to SERTS pointing position 2. The area covered is 1293 × 560 arcsec^2. SERTS intensity contours in lines of (*a*) Fe XVI λ335.4, (*b*) Fe XV λ284.1, (*c*) Mg IX λ368.1, and (*d*) He II λ303.8 are superposed. Intensity contours in ergs cm^{-2} s^{-1} sr^{-1} are (*a*) 100, 200, 400, 600, 800, 1200, 1600, 2500, 4000, 5000; (*b*) 400, 500, 600, 800, 1200, 1600, 2000, 4000, 7000; (*c*) 100, 200, 300, 350, 400, 500, 600, 700; (*d*) 7000, 12000, 15000, 20000, 30000, 50000. The slit-lobe-slit format of the SERTS data is evident, although the intensity contours in the slit portion of these figures should not be taken seriously. The location of the SERTS slit, from which the spatially resolved spectra used in this paper were obtained, is shown in the last frame. NOAA region 7563 is in the upper right of each frame in this figure, and region 7565 is the brightest area left of center. The loop which connects region 7565 with the plage trailing region 7563 is in the center.

BROSIUS et al. (see 477, 971)

FIG. 2*c*

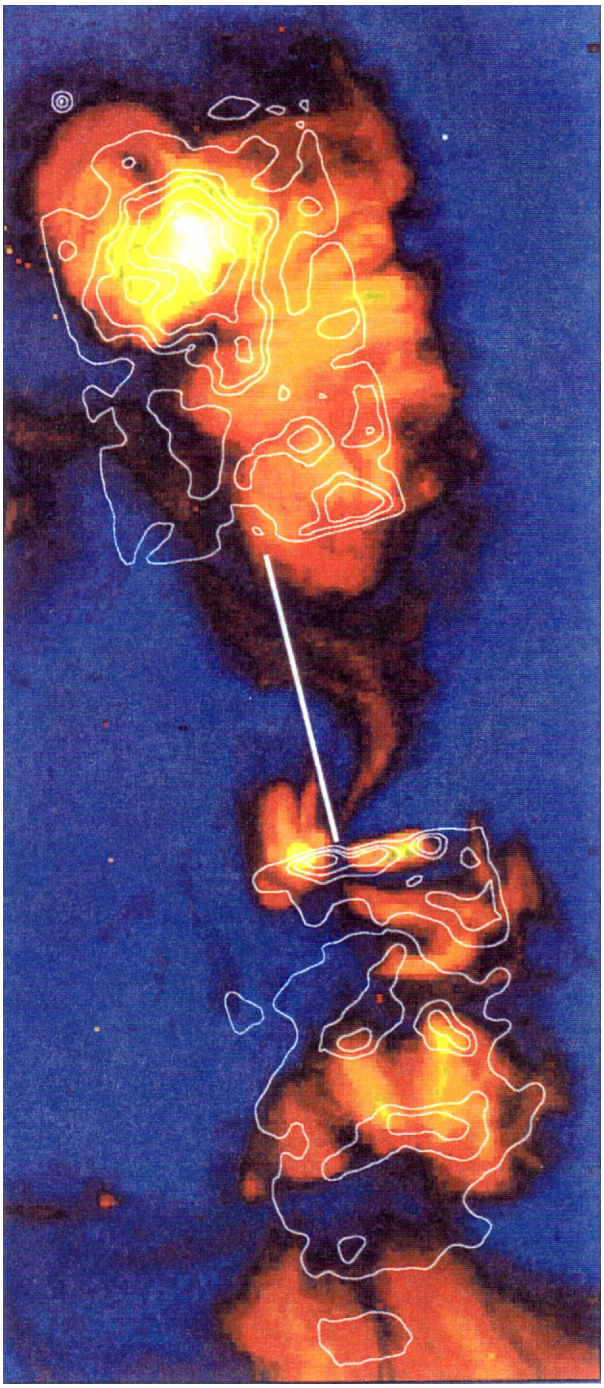

FIG. 2*d*

BROSIUS et al. (see 477, 971)

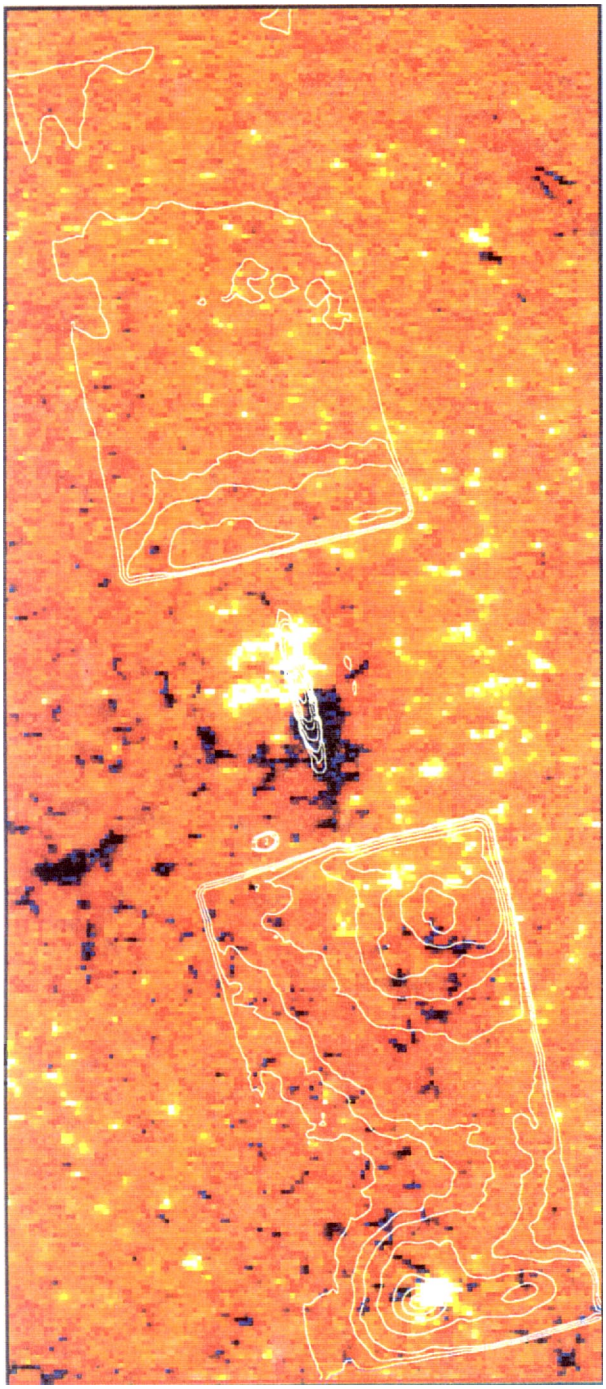

FIG. 3*a*

FIG. 3*b*

FIG. 3.—Kitt Peak photospheric longitudinal magnetogram corresponding to the first SERTS pointing position. SERTS contours of Fe XVI (*top*) and He II (*bottom*) are superposed, with the same levels used in Fig. 1.

BROSIUS et al. (see 477, 972)

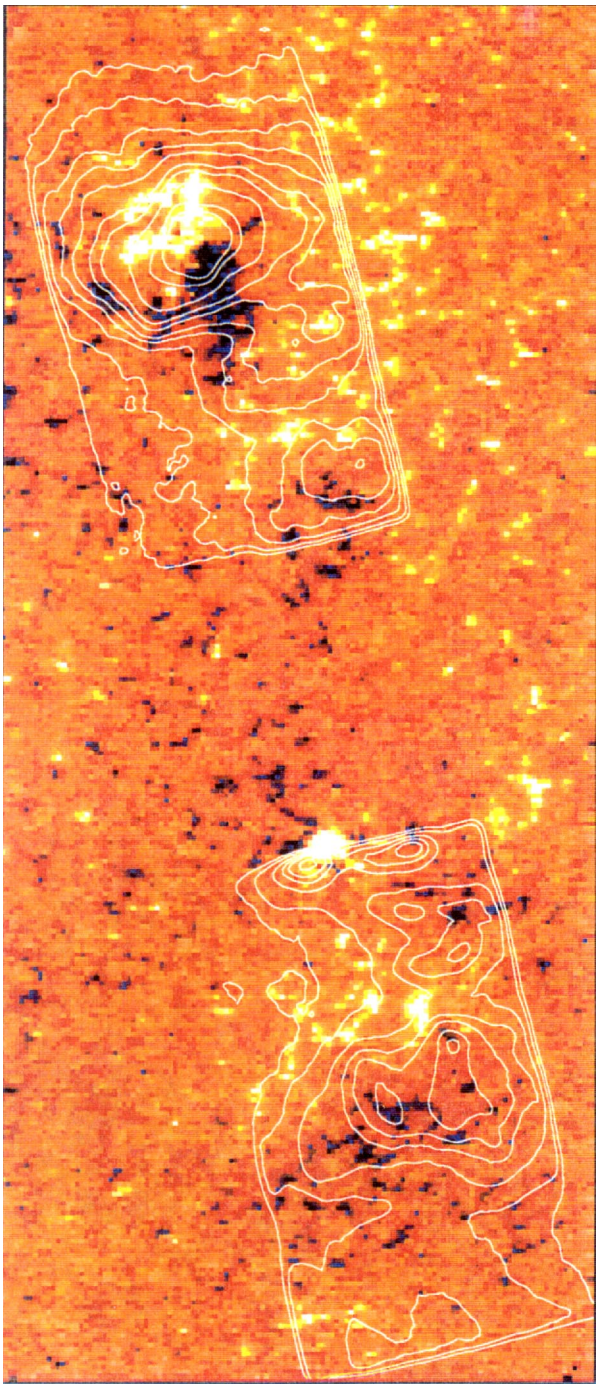

FIG. 4*a*

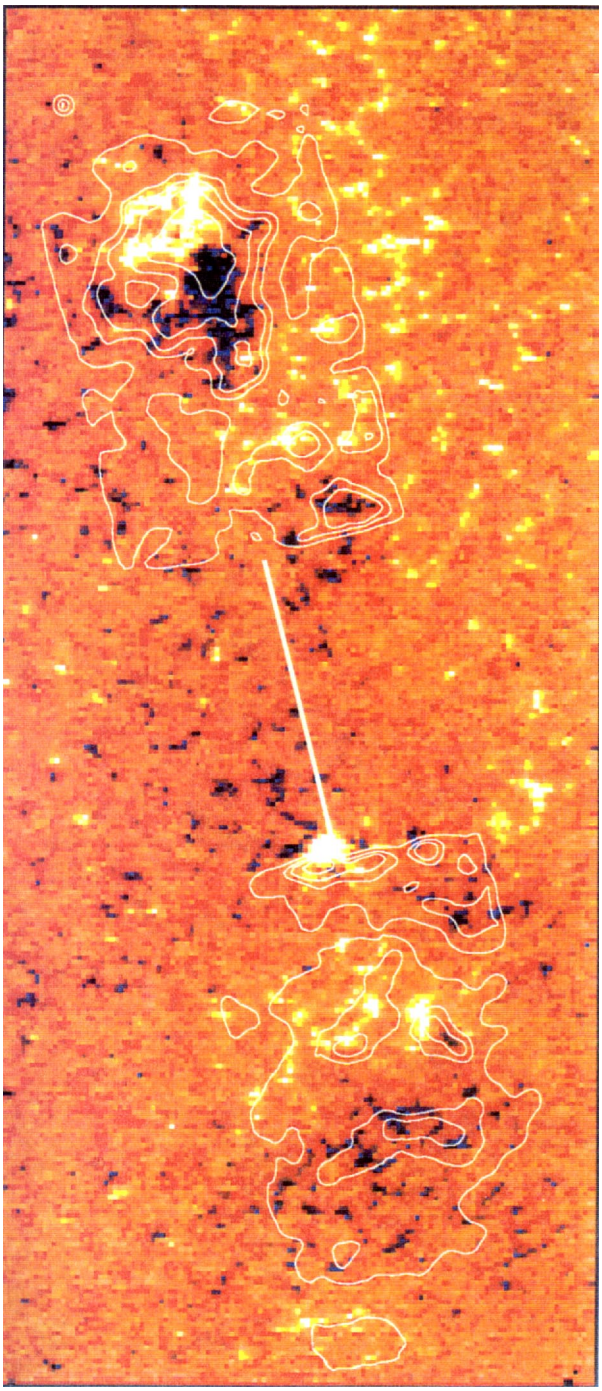

FIG. 4*b*

FIG. 4.—Kitt Peak photospheric longitudinal magnetogram corresponding to the second SERTS pointing position. SERTS contours of Fe XVI (*top*) *and* He II (*bottom*) are superposed, with the same levels used in Fig. 2.